2017

A Test Of The Interstellar Boundary EXplorer Ribbon Formation In The Outer Heliosheath

Konstantin V. Gamayunov

Jacob Heerikhuisen

Hamid K. Rassoul

The Astrophysical Journal, 845:63 (10pp), 2017 August 10 https://doi.org/10.3847/1538-4357/aa7f70

A Test of the *Interstellar Boundary EXplorer* Ribbon Formation in the Outer Heliosheath

Konstantin V. Gamayunov[1], Jacob Heerikhuisen[2,3], and Hamid Rassoul[1]
[1] Department of Physics and Space Sciences, Florida Institute of Technology, Melbourne, FL 32901, USA; kgamayunov@fit.edu
[2] Department of Space Science, University of Alabama in Huntsville, Huntsville, AL 35899, USA
[3] Center for Space Plasma and Aeronomic Research, University of Alabama in Huntsville, Huntsville, AL 35899, USA
Received 2017 May 1; revised 2017 July 10; accepted 2017 July 10; published 2017 August 11

Abstract

NASA's *Interstellar Boundary EXplorer* (*IBEX*) mission is imaging energetic neutral atoms (ENAs) propagating to Earth from the outer heliosphere and local interstellar medium (LISM). A dominant feature in all ENA maps is a ribbon of enhanced fluxes that was not predicted before *IBEX*. While more than a dozen models of the ribbon formation have been proposed, consensus has gathered around the so-called secondary ENA model. Two classes of secondary ENA models have been proposed; the first class assumes weak scattering of the energetic pickup protons in the LISM, and the second class assumes strong but spatially localized scattering. Here we present a numerical test of the "weak scattering" version of the secondary ENA model using our gyro-averaged kinetic model for the evolution of the phase-space distribution of protons in the outer heliosheath. As input for our test, we use distributions of the primary ENAs from our MHD-plasma/kinetic-neutral model of the heliosphere-LISM interaction. The magnetic field spectrum for the large-scale interstellar turbulence and an upper limit for the amplitude of small-scale local turbulence (SSLT) generated by protons are taken from observations by *Voyager 1* in the LISM. The hybrid simulations of energetic protons are also used to set the bounding wavenumbers for the spectrum of SSLT. Our test supports the "weak scattering" version. This makes an additional solid step on the way to understanding the origin and formation of the *IBEX* ribbon and thus to improving our understanding of the interaction between the heliosphere and the LISM.

Key words: ISM: kinematics and dynamics – ISM: magnetic fields – plasmas – scattering – solar wind – turbulence

1. Introduction

The objective of NASA's *Interstellar Boundary EXplorer* (*IBEX*) mission is to obtain a global view of the interaction between the solar wind (SW) and local interstellar medium (LISM; McComas et al. 2009a). This is accomplished by imaging energetic neutral atoms (ENAs) propagating to Earth from the outer reaches of the heliosphere and the nearby parts of the LISM. The *IBEX* spacecraft was launched into a highly elliptical (~15,000 × 300,000 km), ~8 day orbit on 2008 October 19. The mission payload consists of two single-pixel 7° × 7° sensors: *IBEX*-Lo measures ENAs from 0.01 to 2 keV (Fuselier et al. 2009b), and *IBEX*-Hi measures ENAs from 0.3 to 6 keV (Funsten et al. 2009a). The first all-sky maps of ENAs were constructed during the first half of 2009 (McComas et al. 2009b; Funsten et al. 2009b; Fuselier et al. 2009a; Schwadron et al. 2009), and the dominant feature in all maps was a ribbon of enhanced ENA emissions. This ribbon feature had not been predicted by any model and/or theory of the heliospheric interface existing before the *IBEX* era (McComas et al. 2009b; Schwadron et al. 2009). The ribbon is observed from 0.2 to 6 keV with a highest relative intensity at ~1 keV (Fuselier et al. 2009a). The ENA fluxes vary over the ribbon with maxima 2–3 times brighter than those from a surrounding region of more diffuse, globally distributed heliospheric flux (Fuselier et al. 2009a; McComas et al. 2009b). The ribbon is quite narrow in width, having a full width at half maximum (FWHM) of ~10°–40° for ~1 keV and ~40°–70° for ~4 keV (Schwadron & McComas 2013), but long, extending over 300° in the sky (Funsten et al. 2009b; Fuselier et al. 2009a). Figure 1 shows the average ENA flux at 1.11 keV from the seventh *IBEX* data release (McComas et al. 2014), where the two representations of the all-sky map are shown. In the left panel, the direction in the sky is given by ecliptic longitude λ and latitude β. In the right panel, two angles (azimuth, polar) = (θ, ϕ) are shown following Funsten et al. (2013). In this system, the ribbon center (RC) lies at (0°, 0°), and ϕ corresponds to an angle between (0°, 0°) and a point in the sky. The azimuth angle θ ranges from 0° to 360° counterclockwise around the RC. Both panels in Figure 1 show the same ENA flux, but the polar plot reveals a remarkably circular nature of the *IBEX* ribbon.

Presenting the first results from *IBEX*, Funsten et al. (2009b) pointed out that the ribbon location in the sky may be controlled by the interstellar magnetic field (ISMF) orientation. This, combined with the model results for the heliosphere-LISM interaction, allowed Schwadron et al. (2009) to hypothesize that the ISMF, $\boldsymbol{B}$, beyond the heliopause (HP) is nearly transverse to the line of sight (LOS), $\boldsymbol{r}$, from *IBEX* to the ribbon, i.e., $\boldsymbol{B} \cdot \boldsymbol{r} = 0$. This intrinsic ordering by $\boldsymbol{B} \cdot \boldsymbol{r} = 0$ was first formulated by McComas et al. (2009b) as one of the possible mechanisms of the ribbon formation and then quantitatively elaborated by Heerikhuisen et al. (2010). The Heerikhuisen et al. approach is based on the fact that an average SW velocity inside the termination shock (TS) and in the inner heliosheath (IHS) is anti-sunward. So, after charge exchange between the SW/IHS protons and interstellar H, a majority of primary ENAs propagates away from the Sun, and a large portion of them can reach the LISM. The ENAs in the LISM experience charge exchange again, creating energetic protons. These protons propagate along an inhomogeneous ISMF, convect together with the LISM flow in the direction perpendicular to the magnetic field, experience wave-induced pitch angle scattering, and finally, after characteristic charge-exchange time in the LISM, charge exchange with the cold interstellar H, creating secondary ENAs. Then, the sunward propagating fraction of secondary ENAs can be detected by *IBEX*. Following Heerikhuisen et al., this mechanism of the

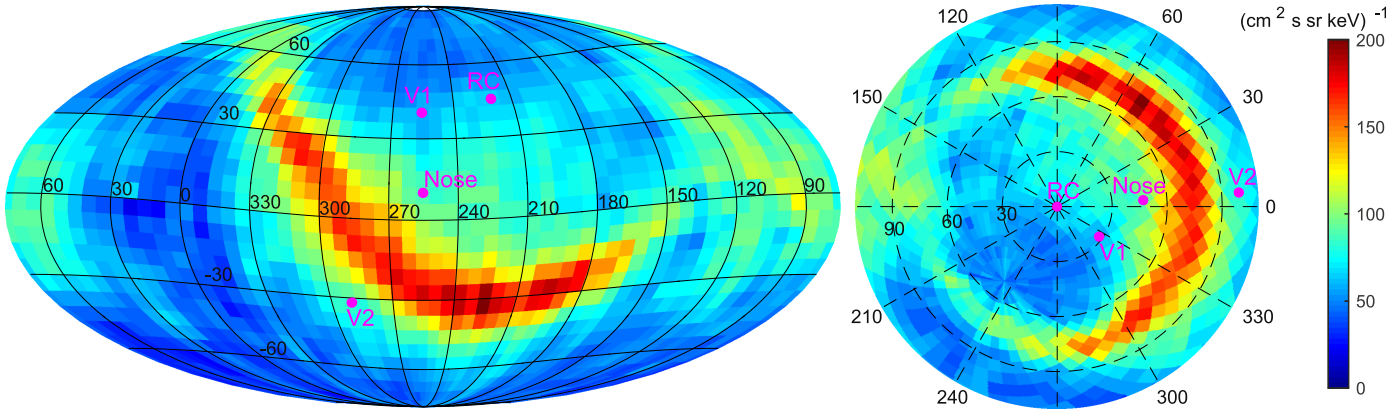

Figure 1. Five-year-averaged ENA flux at 1.11 keV from the seventh *IBEX* data release (McComas et al. 2014). Left: full-sky map in Mollweide projection, where the grid lines are in ecliptic coordinates J2000. The directions to the *Voyager 1* and *2* spacecraft are indicated by *V1* and *V2*, along with the direction from which interstellar-medium flow originates (Nose) and the observed RC at (long., lat.) = (220.°3, 40.°5). Right: polar plot of ENA flux centered on RC that is produced from the left panel using the transformation introduced by Funsten et al. (2013). Note that we use the nose direction from Funsten et al. to align our coordinate axis $\theta = 0°$ in the same way Funsten et al. did, but here we indicate an updated nose direction at (255°, 5°) from McComas et al. (2015).

ribbon formation is called the "secondary ENA" mechanism, and a schematic of it is shown in Figure 1 of McComas et al. (2010).

For the secondary ENA mechanism to be viable, the pitch angle distribution function of energetic protons in the LISM should remain quasi-stable during a characteristic time between two acts of charge exchange that is estimated to be a few years. Otherwise, if pitch angle scattering is faster than charge exchange, the distribution function would be quasi-isotropic, and the secondary ENA mechanism could not produce a narrow ribbon. To avoid this delicate issue, Heerikhuisen et al. (2010) did not simulate the scattering of pickup ions (PUIs) in the LISM but instead introduced the concept of "partial shell" to heuristically approximate the outcome of a limited scattering process between the moment of PUI creation and the moment of its reneutralization. This allowed them to successfully reproduce the overall ribbon structure and many of its properties. Shortly after that, however, Florinski et al. (2010) presented the results of hybrid simulations for an energetic proton ring-beam distribution injected in the LISM, showing that the proton distribution is unstable with respect to a generation of small-scale turbulence, which leads to a nearly isotropic proton distribution on a timescale of only a few days (see also Liu et al. 2012 and Cannon et al. 2014a, 2014b). This has cast doubt on the secondary ENA mechanism as a viable explanation of the ribbon formation. The situation became even less clear after Gamayunov et al. (2010) showed that PUIs in the LISM are stable with respect to small-scale self-generated turbulence, and their pitch angle scattering is mainly controlled by large-scale interstellar turbulence (LSIT). A disagreement between the hybrid and Gamayunov et al. results has precluded a conclusion on the validity of the secondary ENA mechanism. This has also stimulated new ideas on the ribbon formation that are based on a contrary assumption of strong but spatially localized PUI scattering due to the small-scale turbulence locally generated by PUIs in the region of the LISM where $\boldsymbol{B} \cdot \boldsymbol{r} \approx 0$ (Schwadron & McComas 2013; Isenberg 2014), which is leading to the nearly isotropic pitch angle distributions there.

Our knowledge about magnetic field turbulence in the nearby part of the LISM changed dramatically after the *Voyager 1* (*V1*) spacecraft crossed the HP in 2012 and the first in situ observations of the magnetic field in the LISM became available (Burlaga et al. 2014, 2015). These observations first set an upper limit on the amplitude of the small-scale local turbulence (SSLT) generated by PUIs in the LISM (Burlaga et al. 2014). This limit is more than three orders of magnitude below a theoretical prediction from hybrid simulations (Burlaga et al. 2014) and implies that generation of the SSLT is suppressed in the LISM, at least in the *V1* direction. (It is obvious that the SSLT might be generated in the ribbon direction simply because the pitch angles of newly born PUIs depend on the direction, and/or the plasma conditions in the ribbon might be different from those in the *V1* direction.) Second, in situ observations of the LSIT (Burlaga et al. 2015) show that the spectrum of magnetic field fluctuations is close to a Kolmogorov-like power law, being in agreement with the previous remote observations of interstellar turbulence (e.g., Armstrong et al. 1995). This agreement also indicates that characteristics of the LSIT are unlikely to depend on the directions in the LISM. Both the LSIT and SSLT contribute to the pitch angle scattering of PUIs in the LISM, and the rate of this scattering is key to the viability of the secondary ENA mechanism.

Here we present a numerical test of the secondary ENA mechanism. Between two versions of the secondary ENA mechanism, the "strong scattering" version explicitly assumes that PUI scattering by the SSLT is spatially localized in the region of LISM where $\boldsymbol{B} \cdot \boldsymbol{r} \approx 0$. Unfortunately, we currently do not have observations and/or simulation data that may be used to construct the model of the SSLT that reliably treats spatial dependencies in the region of $\boldsymbol{B} \cdot \boldsymbol{r} \approx 0$. So, here we do not test the "strong scattering" version of the secondary ENA mechanism but focus only on the "weak scattering" version. Our analysis is based on the approach used by Gamayunov et al. (2010) with the following modifications. (1) We use distribution functions of the primary ENAs in the LISM from our 3D MHD-plasma/kinetic-neutral model of the heliosphere-LISM interaction (Pogorelov et al. 2004; Heerikhuisen et al. 2005; Heerikhuisen & Pogorelov 2010). (2) The magnetic field spectrum for the LSIT and an upper limit for the amplitude of the SSLT are taken from the *V1* observations in the LISM, though an intensity of the SSLT is not crucial for our analysis (see Section 4 for details). (3) The results of hybrid simulations of PUIs in the direction toward the *IBEX* ribbon are used to set the bounding wavenumbers for the SSLT spectrum.

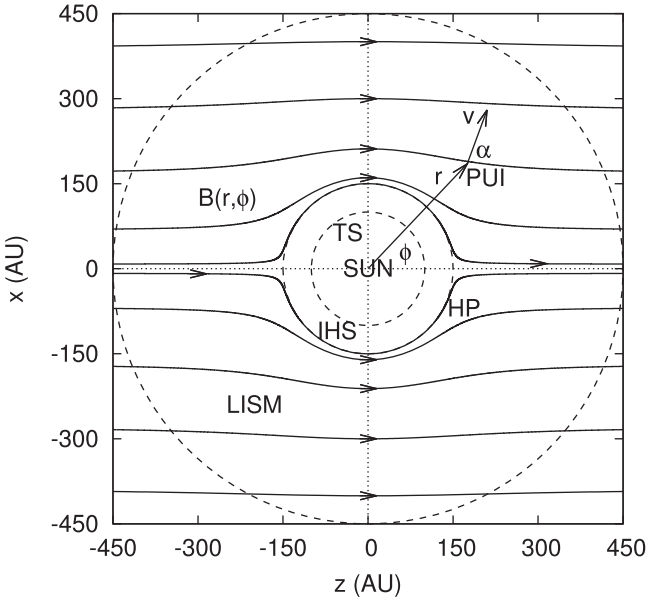

Figure 2. Azimuthal profile of the ISMF used in the modeling of PUI evolution in the LISM. Also shown are schematic locations of the Sun, TS, IHS, HP, and LISM, where three concentric circles depict the TS with radius $r_{TS} = 100$ au, the HP with radius $r_{HP} = 150$ au, and the outer boundary of the simulation domain at $r = 450$ au. A spatial location of PUI is characterized by the length r of its radius vector and the polar angle ϕ measured counterclockwise from the ISMF direction at $z = \infty$. We also show the PUI velocity $\boldsymbol{v}$ and pitch angle α. The shown magnetic field maximizes at $(r, \phi) = (r_{HP}, \pm 90^{\circ})$, and we set the magnetic field at these locations to 4.8 μG in accordance with the *V1* observations in the LISM (Burlaga et al. 2014). Note that the ISMF model adopted here translates the above magnetic field at the HP to 3.2 μG at infinity.

2. Model of Energetic Protons in the LISM

In the secondary ENA model, the ribbon ENA emissions originate in the LISM due to a charge exchange between energetic (~keV) protons and interstellar H. The energetic protons are initially supplied in the LISM in the form of primary energetic H, which is produced by charge exchange between the SW and/or IHS protons and interstellar H in the heliosphere. The energetic H is then charge-exchanged with the cold LISM protons, creating an energetic proton population in the LISM. Figure 2 shows an azimuthal cut of the ISMF used in this study, along with schematic locations of the Sun, TS, IHS, HP, and LISM. The used magnetic field results from the interaction of the SW and LISM in an extreme case when both the interstellar gas and dynamic pressures are insignificant compared to the ISMF pressure (Parker 1961). This limit was considered by Parker (1961) as one of the two possible extremes of interaction between the stellar wind and ISMF. In a leading approximation, the magnetic field in this limit is given by a superposition of the dipole magnetic field and a constant ISMF oriented antiparallel to the magnetic moment of dipole. This leading approximation is shown in Figure 2 (the equation for magnetic field in Figure 2 can be found, for example, in Gamayunov et al. 2010). For clarity, however, note that *IBEX* observations suggest that both the ISMF pressure and the LISM dynamic/kinetic pressure are important in shaping the outer heliosphere (McComas et al. 2009b). So a real magnetic field configuration in the LISM is likely to be something in between the two extremes analyzed by Parker (1961). Nevertheless, for the purpose of this study, to test the existence of the secondary ENA mechanism, a pitch angle scattering of PUIs in the LISM is the most crucial element of the analysis but not the ISMF configuration. So it is methodologically correct to use as simple a magnetic field model as possible.

In this study, we will model the PUI evolution in the plane formed by two straight lines from the Sun; one line is directed to the RC (see Figure 1), and the second line has the ecliptic J2000 direction (250°, −25.°25). The inner boundary of the PUI simulation domain is placed at the radial distance to the HP, $r_{HP} = 150$ au. To allow sufficient distance for the charge exchange in the LISM, the outer boundary is placed at $r = 450$ au, and particle inflow through the outer boundary is neglected. All the technical details on modeling energetic protons and calculation of the ENA fluxes from the LISM are given in Sections 2.1 and 2.2. Here we only emphasize that the phase-space distribution function (PSDF) of the primary energetic H in the LISM is obtained from our 3D MHD-plasma/kinetic-neutral model of the heliosphere-LISM interaction (Pogorelov et al. 2004; Heerikhuisen et al. 2005; Heerikhuisen & Pogorelov 2010). To calculate the pitch angle diffusion coefficient for energetic protons, the magnetic field spectra for both the LSIT and SSLT are constructed from the *V1* observations in the LISM (Burlaga et al. 2014, 2015) and the results of hybrid simulations. Then, a stationary solution of the governing equation for energetic protons is obtained. Finally, using this solution, the ENA flux from the LISM is calculated at the *IBEX* location.

2.1. Governing Equation for Energetic Protons

We use the gyro-averaged kinetic equation for the proton PSDF $f(\boldsymbol{x}, \boldsymbol{p}, t)$ used by Gamayunov et al. (2010):

$$\frac{\partial f}{\partial t} + v\mu b_i \frac{\partial f}{\partial x_i} + \frac{(1-\mu^2)}{2} v \frac{\partial b_i}{\partial x_i} \frac{\partial f}{\partial \mu} = \frac{\partial}{\partial \mu}\left(D_{\mu\mu} \frac{\partial f}{\partial \mu} \right) + P - L. \quad (1)$$

Here v, μ, and $\boldsymbol{b}$ are the proton speed, pitch angle cosine, and unit magnetic field vector, respectively, and the number density of protons in the phase-space element is given by the equation $dn(\boldsymbol{x}, \boldsymbol{p}, t) = f(\boldsymbol{x}, \boldsymbol{p}, t) 2\pi p^2 dp d\mu$. The three terms in the right-hand side of Equation (1) describe the wave-induced pitch angle scattering with the diffusion coefficient $D_{\mu\mu}$ and the proton production (P) and loss (L) due to the charge exchange. Equation (1) is written in a mixed-coordinate frame, where the spatial coordinate $\boldsymbol{x}$ is measured in the solar frame and momentum $\boldsymbol{p}$ is measured in the frame comoving with the LISM bulk flow. Here, however, we consider the proton energies about 1 keV, and so the difference between the solar and mixed frames may be ignored because the LISM flow speed is about 21–26 km s^{-1} (McComas et al. 2012). This is negligible compared to the proton speed of ~430 km s^{-1} for the 1 keV proton.

The production and loss terms in Equation (1) have the forms (Heerikhuisen et al. 2008)

$$P(\boldsymbol{x}, \boldsymbol{p}, t) = f_H(\boldsymbol{x}, \boldsymbol{p}, t) \sigma_{ex}(v) v n_{p,LISM}, \quad (2)$$

$$L(\boldsymbol{x}, \boldsymbol{p}, t) = f(\boldsymbol{x}, \boldsymbol{p}, t) \sigma_{ex}(v) v n_{H,LISM}, \quad (3)$$

where f_H is the PSDF of the primary energetic H in the LISM, σ_{ex} is the H–p charge-exchange cross section, $n_{p,LISM}$ is the number

density of the cold interstellar protons, and $n_{\rm H,LISM}$ is the number density of the cold H in the LISM. The PSDF of the primary energetic H is obtained from our 3D MHD-plasma/kinetic-neutral model of the heliosphere-LISM interaction (Pogorelov et al. 2004; Heerikhuisen et al. 2005; Heerikhuisen & Pogorelov 2010). For both densities in Equations (2) and (3), we also use results from our 3D model, and $n_{p,\rm LISM} = 1.18 \times 10^{-1}\,{\rm cm}^{-3}$ and $n_{\rm H,LISM} = 2.03 \times 10^{-1}\,{\rm cm}^{-3}$ are adopted in this study. The energy-dependent charge-exchange cross sections are taken from Barnett (1990), where $\sigma_{\rm ex} \approx 2 \times 10^{-15}\,{\rm cm}^2$ for the proton energy $\sim$1 keV. The characteristic timescales for production of the 1 keV protons in the LISM, $\tau_P = (\sigma_{\rm ex} v n_{p,\rm LISM})^{-1}$, and their loss, $\tau_L = (\sigma_{\rm ex} v n_{\rm H,LISM})^{-1}$, are about $\tau_P \approx 3.1$ and $\tau_L \approx 1.8$ yr, and the mean free path for the primary energetic H without charge exchange beyond the HP is $L_H = (\sigma_{\rm ex} n_{p,\rm LISM})^{-1} \approx 280$ au. It also follows from our MHD-plasma/kinetic-neutral model that the densities of the primary energetic neutrals decrease with radial distance (due to a combination of spherical expansion and extinction) beyond the HP as $\sim 1/r^{2.7}$ and $\sim 1/r^{3.3}$ for neutrals originating upstream of the TS and inside the IHS, respectively (Heerikhuisen et al. 2016).

A widely used quasi-linear approximation for the pitch angle diffusion coefficient is used in this study. The Alfvén and fast magnetosonic waves propagating parallel and antiparallel to the ISMF are most effective in the particle pitch angle scattering, and only these waves are taken into account in the diffusion coefficient. For the case of gyroresonant scattering of energetic protons by the field-aligned waves, we use the diffusion coefficient derived by Schlickeiser (1989) and given by Equation (45) of that paper. The magnetic field spectra for both the large- and small-scale turbulence that are needed to calculate the diffusion coefficient are constructed from the *V1* observations in the LISM (Burlaga et al. 2014, 2015) and the results of hybrid simulations (see Section 4). Note that we use the spectra of the total magnetic field fluctuations observed by *V1*, including the compressional component of the magnetic field that does not contribute to the pitch angle scattering. So the diffusion coefficient used here is slightly overestimated by a factor of about 2.

Finally, the details and references of the numerical schemes used to solve Equation (1) can be found in Gamayunov et al. (2010).

2.2. ENA Flux from the LISM

The ENA flux from the LISM observed at the *IBEX* location, which is approximately the Sun location, in the radial direction $\boldsymbol{n}$ can be obtained by collecting the respectively directed and weighted proton fluxes in the LISM along the LOS. In the solar frame, at the Sun location, and neglecting the velocity of the cold interstellar H, the resulting flux of the ENAs can be written as (e.g., Gruntman et al. 2001)

$$j_{\rm ENA}(\boldsymbol{n}, p) = \int_{r_{\rm HP}}^{\infty} dr j(r, \boldsymbol{n}, p) \sigma_{\rm ex}(v) n_{\rm H,LISM}(r), \qquad (4)$$

where integration along the LOS is extended over the entire radial extent beyond the HP, and $j(r, \boldsymbol{n}, p) = p^2 f(\boldsymbol{x}, \boldsymbol{p}, t)$ is the flux of energetic protons in the LISM. In Equation (4), we take a survival probability to be unity (Gruntman et al. 2001) and so neglect the ENAs' extinction on their way from the point of birth to the observational point. This allows for direct comparisons to the *IBEX* data products, which provide fluxes where such losses have been added back in.

3. Distribution of Primary ENAs in the LISM

To have a source of energetic protons in the LISM that is as realistic as possible, we use the PSDF of the primary energetic H in the LISM obtained from our global 3D MHD-plasma/kinetic-neutral model of the heliosphere-LISM interaction (Pogorelov et al. 2004; Heerikhuisen et al. 2005; Heerikhuisen & Pogorelov 2010). The MHD-neutral model is based on an MHD description of plasma coupled to a kinetic particle code for H. The particle motions are subject to the H-proton charge exchange that results in a loss of H atoms and simultaneous gain of new H atoms that were previously protons. The probability of charge exchange depends on the proton velocity distribution, and the protons are assumed to follow a Maxwellian distribution except in the IHS, where a κ-distribution (e.g., Livadiotis & McComas 2013) with $\kappa = 1.63$ is used to take into account the presence of suprathermal PUIs (Heerikhuisen et al. 2008).

A total population of neutrals in the LISM can be decomposed into three components, depending on the plasma conditions in which the neutrals are generated. The first component is made up of the cold interstellar neutrals, and sometimes this component is further subdivided into pristine neutrals and neutrals disturbed by the presence of the heliosphere. The second component is generated in the IHS, where the plasma is hot and newly born ENAs propagate in all directions. The third component ENAs are produced in the supersonic SW, upstream of the TS. These ENAs only travel away from the Sun and are sometimes referred to as the neutral SW.

In this study, we model the PUI evolution in the plane formed by two straight lines from the Sun; one line is directed to the RC, and the second line has the ecliptic J2000 direction (250°, −25.°25) from which strong ribbon emissions are observed. As an example, Figure 3 shows the gyro-averaged velocity distribution functions of the primary ENAs in the LISM at the radial distance 157.5 au and in the ecliptic J2000 direction (250°, −25.°25). The distributions of ENAs born in the supersonic SW and the IHS are shown in the left and right panels, respectively. The distributions in Figure 3 are obtained from the Heerikhuisen et al. (2014) simulation, where the ISMF at infinity is 3 μG, which is close to the magnetic field at infinity in Figure 2. The hydrogen component is modeled as a large ensemble of particles that can be reduced to the hydrogen PSDF on a 6D space-velocity grid (Heerikhuisen & Pogorelov 2010). The grid data are then transformed into the LISM plasma frame and gyro-averaged about the local magnetic field. The ENAs born in the supersonic SW are given a radial speed according to their heliolatitude and a randomly selected time from the data set produced by Sokól et al. (2013). This allows a steady-state solution to include a time-averaged distribution of radial speeds for the neutral SW. The temperature of the ENAs produced in the supersonic SW is set as a function of radial distance from the Sun according to the core SW temperature (Gamayunov et al. 2012) measured by the *V2* spacecraft. Additionally, at distances less than 1 au, we use an adiabatic temperature profile $T(r) = T(1\ {\rm au}) r^{-4/3}$, while for distances beyond 84 au, where *V2* encountered the TS, we apply the *V2* average of the last 10 au before the TS (≈15,000 K). Also,

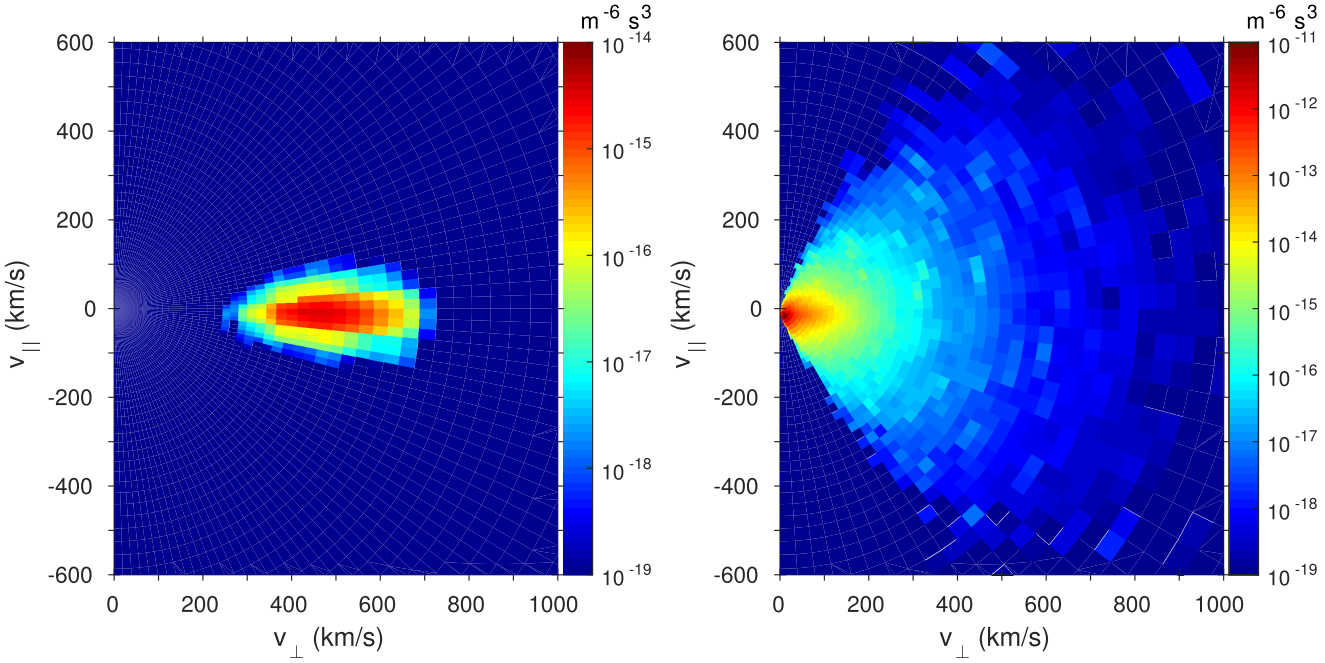

Figure 3. Gyro-averaged distribution functions of the primary ENAs in the LISM at the radial distance 157.5 au in the ecliptic J2000 direction (250°, −25°.25). The distributions of ENAs born in the supersonic SW and the IHS are shown in the left and right panels, respectively. The ENA velocities are measured in the frame comoving with the LISM bulk flow, and components parallel and perpendicular to the ISMF are shown. Note that the number densities calculated from the left and right distributions are $n \approx 3.5 \times 10^{-5}$ cm^{-3} and $n \approx 3.5 \times 10^{-4}$ cm^{-3}, respectively.

while the thermal spread of ENAs perpendicular to their bulk radial motion in the left panel of Figure 3 is overestimated due to a resolution restriction imposed by the current model grid (the temperature is overestimated by a factor of ∼2.5, and the distribution has a temperature along the ISMF of ∼49,000 K), this does not affect the results of our analysis below because, as will be shown, the resulting ribbon widening is mainly controlled by the scattering of energetic protons in the LISM but not thermal spread in the primary ENA distributions. Finally, the ENA distribution in the right panel of Figure 3 is obtained using a κ-distribution for the IHS protons. For a more in-depth analysis of the neutral atom properties in the direction toward the *IBEX* ribbon, see Heerikhuisen et al. (2016).

4. Spectra of the Large- and Small-scale Turbulence in the LISM

The *V1* observations of both the large- and small-scale magnetic field fluctuations in the LISM give us the data needed to realistically test the secondary ENA mechanism. The previous remote observations of the LSIT show that the spectrum of the electron density fluctuations is close to a Kolmogorov-like power law ($\sim k^{-5/3}$) in a broad wavenumber range of $k \sim 10^{-19}$–10^{-8} cm^{-1} (Armstrong et al. 1995; Chepurnov & Lazarian 2010). The electron density fluctuations can be connected to the magnetic field fluctuations, according to Montgomery et al. (1987; see also the summary and conclusions section in Armstrong et al. 1995). Due to fluctuations in the fluid ram and magnetic pressures, an incompressible MHD turbulence has second-order ponderomotive density fluctuations (e.g., Gamayunov & Khazanov 1995), and the spectrum of density fluctuations is proportional to the spectrum of magnetic fluctuations.

Using the best-fit estimates from the *V1* observations, the magnetic field spectrum for the LSIT can be written as

$$B^2_{\rm LS}(k) = 0.5 \frac{\langle \delta B^2_{\rm LS} \rangle}{k_{\rm min}\,(1 + k^{5/3}/k^{5/3}_{\rm min})}, \qquad (5)$$

where wavenumber k is positive, $\langle \delta B^2_{\rm LS} \rangle = 9 \times 10^{-12}$ G^2, $k_{\rm min} = 2\pi/10$ ps^{-1} (Burlaga et al. 2015), and normalization is $\int_0^\infty B^2_{\rm LS}(k)dk = \langle \delta B^2_{\rm LS} \rangle$. In the calculations of diffusion coefficients, the spectral density in Equation (5) is equally split between waves propagating parallel and antiparallel to the ISMF and between Alfvén and fast magnetosonic waves. Part of the LSIT spectrum in Equation (5) is shown in Figure 4. Note that the above values for $\langle \delta B^2_{\rm LS} \rangle$ and $k_{\rm min}$ are not uniquely specified by the fit of $B^2_{\rm LS}(k)$ to the *V1* observations. This fact, however, is unimportant for our study, because $B^2_{\rm LS}(k)$ should fit the *V1* observations for any choice of the pair $\langle \delta B^2_{\rm LS} \rangle$ and $k_{\rm min}$, and the wavenumbers resonating with PUIs are much larger than the wavenumbers covered by the *V1* observations of the LSIT (see below).

The *V1* observations of the LSIT cover only the wavenumber range $\sim 10^{-13}$–10^{-11} cm^{-1} (Burlaga et al. 2015), and extrapolation of a power law into the region of higher wavenumbers is based on the remote observations of interstellar turbulence (Armstrong et al. 1995). It is likely, however, that the LSIT spectrum has rollover at wavenumbers $\sim 10^{-8}$ cm^{-1} or so. By assuming the $\sim k^{-5/3}$ spectrum in the region of large wavenumbers, we increase the energetic proton scattering rate in the region around the 90° pitch angle and so create a more difficult situation to survive for the secondary ENA mechanism based on a weak PUI scattering. Thus, if this secondary ENA

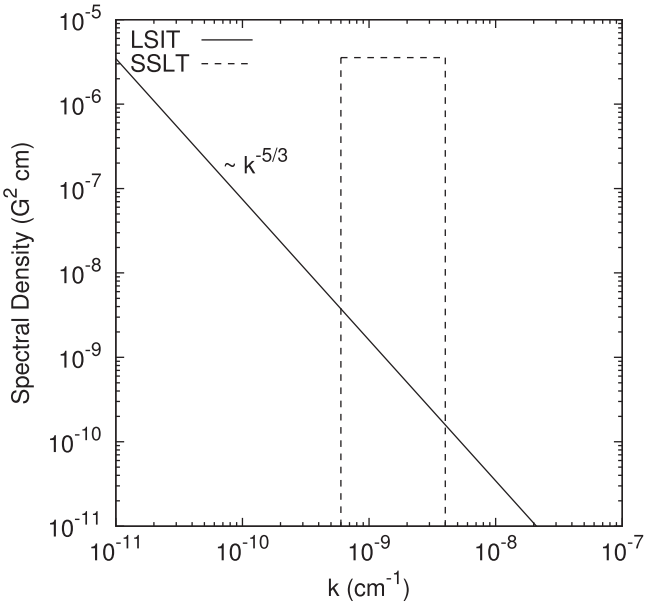

Figure 4. Spectral density of the ISMF fluctuations vs. wavenumber estimated from the *V1* measurements in the LISM (Burlaga et al. 2014, 2015). Spectra for both the LSIT and SSLT are shown. A Kolmogorov-like power law ($\sim k^{-5/3}$) for the LSIT is observed in a broad wavenumber range of $k \sim 10^{-19}$–10^{-8} cm^{-1} (Armstrong et al. 1995; Chepurnov & Lazarian 2010), but only a small fraction of the spectrum is shown here. The best-fit estimates from the *V1* observations give $L = 10$ ps $= 3 \times 10^{19}$ cm and $\langle \delta B^2_{\rm LS} \rangle = 9 \times 10^{-12}$ G^2 for the outer scale and energy density of the LSIT, respectively.

mechanism still exists in the framework of this model setup, it means that this mechanism can function in the real LISM conditions.

The intensity of the SSLT can be estimated from the *V1* magnetic field measurements of 48 s averages during each day (Burlaga et al. 2014). These measurements give $\langle \delta B^2_{\rm SS} \rangle^{1/2} = 0.11 \pm 0.09$ μG, which is comparable to the intrinsic instrument uncertainty of 0.09 μG due to magnetometer noise and digitization level (Burlaga et al. 2014). Observation of the SSLT essentially at the instrument threshold does not allow one to perform a reliable spectral decomposition, and only an upper limit for the amplitude of the SSLT is known. To estimate the wavenumber domain for the SSLT, we may use the limiting wavenumbers for the magnetic field spectrum resulting from the 1D hybrid simulation that is shown in the inset of Figure 10 in Burlaga et al. (2014). The shown spectrum is obtained from a hybrid simulation of the proton distribution similar to that in the left panel of Figure 3 that is injected into the LISM plasma perpendicular to the ISMF. This spectrum has a nearly flat shape in the wavenumber domain between $k_1 \approx 6 \times 10^{-10}$ cm^{-1} and $k_2 \approx 4 \times 10^{-9}$ cm^{-1}, and the "tail" in the region $k > k_2$ is entirely due to a computational noise in the hybrid simulation and is thus unphysical. A potential turbulent energy cascade in the region of larger wavenumbers, which is suppressed in 1D simulations, is also unlikely to transport the essential energy of the SSLT into the region $k > k_2$. Indeed, recent 2D full particle-in-cell (PIC) simulations of an energetic proton ring distribution injected in the direction toward the ribbon show that the dominant modes propagate parallel to the magnetic field, and fluctuations progressively migrate from larger to smaller k (see Figure 7 in Niemiec et al. 2016). These PIC results are in agreement with the results of 1D hybrid simulations.

The following arguments suggest that the above limiting wavenumbers k_1 and k_2 are likely to specify a widest wavenumber domain for the SSLT in the ribbon direction. The intensity of the SSLT measured by *V1* is more than three orders of magnitude below the prediction from the hybrid simulation, and, in our arguments, we assume that the "real" intensity of the SSLT in the ribbon is between the *V1* observations, i.e., $\langle \delta B^2_{\rm SS} \rangle$, and the "hybrid simulation" intensity. In the case of the "hybrid simulation" intensity, we simply have the above limiting wavenumbers k_1 and k_2 that are dictated by the 1D hybrid simulations. If the other limiting case takes place, i.e., if the intensity of the SSLT is close to that of the *V1* observations, it implies that much less free energy initially available in the ring distribution of PUIs goes into a generation of waves compared to the case of hybrid simulation. In other words, a range of pitch angles where an initial PUI ring distribution evolves into a quasi-isotropic distribution is wider in the case of the hybrid simulation than in the case of $\langle \delta B^2_{\rm SS} \rangle$. This also means that a wavenumber domain of the SSLT resulting from the hybrid simulation is larger because the resonance conditions between energetic protons and Alfvén and fast magnetosonic waves link the proton pitch angles and wavenumbers (see below in this section). It follows from the resonance conditions that a wider pitch angle range of the resonating protons requires a wider wavenumber domain for waves interacting with the protons.

Now, if we place the entire energy density of the SSLT observed by *V1* in the wavenumber region $k = [k_1, k_2]$, we again create a more difficult situation to survive for the secondary ENA mechanism based on a weak PUI scattering. The resulting spectrum for the SSLT is

$$B^2_{\rm SS}(k) = \frac{\langle \delta B^2_{\rm SS} \rangle}{(k_2 - k_1)} \qquad (6)$$

for $k_1 \leqslant k \leqslant k_2$ and $B^2_{\rm SS}(k) = 0$ otherwise. Spectrum (6) is shown in Figure 4, and it will be used in this study. Similar to Equation (5), the spectrum in Equation (6) is also equally split between waves propagating parallel and antiparallel to the ISMF and between Alfvén and fast magnetosonic waves in order to calculate the diffusion coefficients. Note that recent, more advanced hybrid simulations with exceptionally high particle statistics by Florinski et al. (2016) showed that the PUI distribution function injected in the direction toward the *IBEX* ribbon is stable if this distribution has a temperature along the ISMF that is greater than ~500 K but less than the temperature of the core protons in the LISM. This is the result that was originally obtained by Gamayunov et al. (2010) from simple estimates. A temperature below 500 K is clearly not the case for distributions of the primary ENAs born in the supersonic SW and/or in the IHS. However, the parallel temperature of ENAs born in the supersonic SW and injected in the direction toward the *IBEX* ribbon is likely to be below the temperature of the core protons in the LISM. If the parallel temperature of the PUI distribution is larger than the temperature of the core protons, the PUI distribution is unstable, and the generated SSLT is confined in the wavenumber region $k \approx [k_1, k_2]$ (see Figure 7 in Florinski et al. 2016). This case is also shown in the inset of Figure 10 in Burlaga et al. (2014; as we noted in Section 3, the parallel temperature in the left panel of Figure 3 is overestimated, being larger than the core proton temperature

in the LISM). So the limiting wavenumbers k_1 and k_2 adopted for the SSLT spectrum in Figure 4 will indeed result in the largest possible PUI scattering in the ribbon.

The resonance conditions between energetic protons and waves are $\omega - kv_{\parallel} \mp \Omega_p = 0$ (e.g., Kennel & Petschek 1966), where $\omega = kV_A$ is the wave frequency in the low-frequency approximation for field-aligned propagation, V_A is the Alfvén speed, $v_{\parallel}$ is the component of proton velocity parallel to the ISMF, Ω_p is the proton gyrofrequency, and sign "−" or "+" should be taken for Alfvén or fast magnetosonic waves, respectively. Note that we may use the low-frequency approximation in the adopted wavenumber region $k = [k_1, k_2]$ because $k_2 V_A/\Omega_p \approx 0.3$, and so the normalized difference between the full dispersion relation and low-frequency approximation is $|\omega(k) - kV_A|/kV_A < 0.15$. The above resonance conditions immediately give us the largest possible range of proton pitch angles that can resonate with the SSLT. This range is given by inequalities $V_A/v[\Omega_p/(k_2V_A) - 1] \leqslant |\cos\alpha| \leqslant \min\{V_A/v[\Omega_p/(k_1V_A) + 1], 1\}$, and there is no wave-particle interaction for $V_A/v[\Omega_p/(k_2V_A) - 1] > 1$. In the LISM, $\Omega_p = 4.5 \times 10^{-2}$ rad s^{-1} and $V_A = 30.2$ km s^{-1} are typical, and the above inequalities for the 1 keV protons ($v = 433.9$ km s^{-1}) take the form $0.19 \leqslant |\cos\alpha| \leqslant 1$. This means that the 1 keV protons with pitch angles $79° < \alpha < 101°$ do not interact with the SSLT independently of the turbulence intensity. Only Alfvén waves with wavenumbers in the "tail" region of the spectrum ($k > k_2$) can potentially scatter energetic protons with pitch angles around 90°. Waves in this wavenumber region, however, can only be generated in the case of very cold distributions of the primary ENAs with temperatures along the ISMF less than ∼500 K (Florinski et al. 2016). As we emphasize above, this is not the case. A turbulent energy cascade is also unlikely to transport an essential part of the SSLT energy into the region $k > k_2$ (Niemiec et al. 2016).

We also have to recall here that *V1* is measuring the magnetic fluctuations in a different radial direction than the direction toward the *IBEX* ribbon (see Figure 1). So, in principle, the characteristics of the SSLT generated by PUIs could potentially depend on the direction in the LISM, because the pitch angles of newly born PUIs depend on that direction. We, however, use the bounding wavenumbers k_1 and k_2 resulting from hybrid simulations of PUIs in the direction toward the ribbon but not from observations. So, as far as the bounding wavenumbers exist, the direction of observation does not make a big difference, because the SSLT does not scatter energetic protons with pitch angles around 90° independently of the turbulence intensity. Also, the change of intensity of the SSLT does not change the physical situation qualitatively, as far as the scattering by the SSLT stays faster than the scattering by the LSIT.

5. Test of the Secondary ENA Mechanism

The *IBEX* ribbon is most pronounced for the ENA energies around 1 keV (McComas et al. 2009b), and for our test we only consider the *IBEX*-Hi energy passband with the nominal energy 1.11 keV. The pitch angle scattering of PUIs in the LISM is a key element for viability of the secondary ENA mechanism, and Figure 5 shows the model pitch angle distributions of the 1.11 keV protons in the LISM at the radial distance 198 au. The distributions are shown for three polar angles: $\phi = 90.^{\circ}5$ (a), $\phi = 82.^{\circ}5$ (b), and $\phi = 70.^{\circ}5$ (c). For each ϕ direction, the model profiles are shown for the four scenarios of the proton pitch angle diffusion in the LISM: no diffusion (No Diff) and diffusion due to the SSLT only (SSLT), the LSIT only (LSIT), and the composite LSIT and SSLT (LSIT+SSLT). It follows from Figure 5 that the LSIT controls pitch angle scattering around 90°, where no resonance interaction between protons and the SSLT takes place (see Section 4), but the SSLT determines scattering outside the pitch angle region around 90°. All pitch angle distributions shown in Figure 5 are highly anisotropic independently of the scattering scenario used in the model. A decrease of the polar angle in Figures 5(b) and (c) leads to an obvious shift of the distribution peak into the region of smaller pitch angles (see Figure 2). This shift increases the speed of proton outflow from the system. At the same time, a proton inflow from the region of higher polar angles also increases with a decrease of ϕ. A balance between these two competing processes mainly determines the resulting peaks in the "No Diff" cases shown in Figures 5(b) and (c). The effect of mirror force in Equation (1) should also be invoked in order to understand the profile widening and development of an asymmetry around the peak. This effect is especially seen in the "No Diff" case in Figure 5(c). Both the SSLT and LSIT in Figures 5(b) and (c) work similar to those in Figure 5(a).

To show the dependencies of the 1.11 keV proton number density on the polar angle, we integrated over pitch angles the PSDFs of the 1.11 keV protons at the radial distance 198 au. Figure 6 shows the results of integration for the four scenarios of proton pitch angle diffusion in the LISM. The existence of the LSIT is firmly established by both the remote and in situ observations. So the cases of "No Diff" and "SSLT" are unrealistic and are shown in Figure 6 for contrast against the cases with the LSIT. For the cases of "LSIT" and "LSIT+SSLT", the polar angle profiles in Figure 6 have a minimum in the direction of $\phi = 90°$, i.e., in the direction of $\boldsymbol{B} \cdot \boldsymbol{r} = 0$. An increase in number density with a decrease in ϕ is due to an increase in the contribution of the proton inflow from the region of higher polar angles.

Next, we show the model ENA fluxes at the Sun location. The left panel of Figure 7 shows the results for energy 1.11 keV, where ENA fluxes versus polar angle in the azimuthal plane are shown at the Sun/*IBEX* location. As before, the model profiles are shown for the four scenarios of the proton pitch angle scattering in the LISM. The cases of "No Diff" and "SSLT" are close to each other because the SSLT does not scatter energetic protons with pitch angles close to 90°. The FWHM for these two cases is ∼3°, which is much smaller than the observed FWHMs of ∼15°–25° for a "pure ribbon" after the diffuse globally distributed heliospheric flux is removed from the *IBEX* observations (Fuselier et al. 2009a; Schwadron et al. 2014). The reader should not be confused by the large discrepancy between the observed and modeled FWHMs. As we already emphasized above, the existence of the LSIT is firmly established by both the remote and in situ observations, and so the cases of "No Diff" and "SSLT" are unrealistic and shown here for contrast against the cases with the LSIT. For two other cases, "LSIT" and "LSIT+SSLT", the respective FWHMs are ∼17° and ∼13°, which are in the range of the observed FWHMs. The results for "LSIT" and "LSIT+SSLT" shown in the left panel of Figure 7 are the major results of our test. Here we have used the *V1*

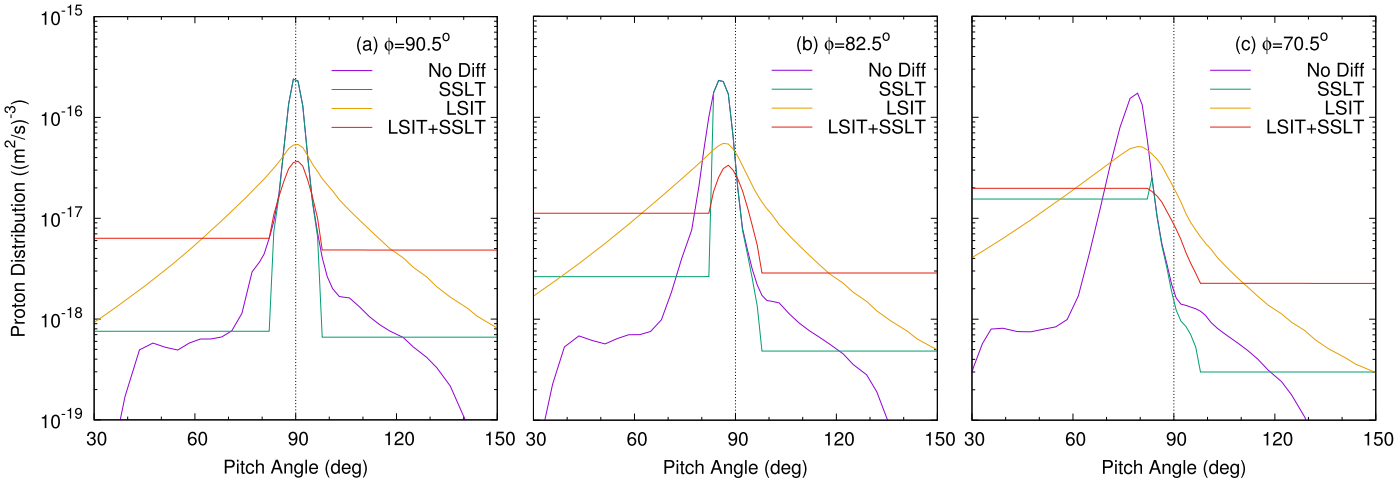

Figure 5. Model distributions of the 1.11 keV protons in the LISM at the radial distance 198 au and for three polar angles: $\phi = 90.^{\circ}5$ (a), $\phi = 82.^{\circ}5$ (b), and $\phi = 70.^{\circ}5$ (c). For each direction, the four pitch angle profiles are shown: for the case of no pitch angle diffusion of energetic protons (No Diff) and for diffusion due to the SSLT only, LSIT only, and composite LSIT+SSLT.

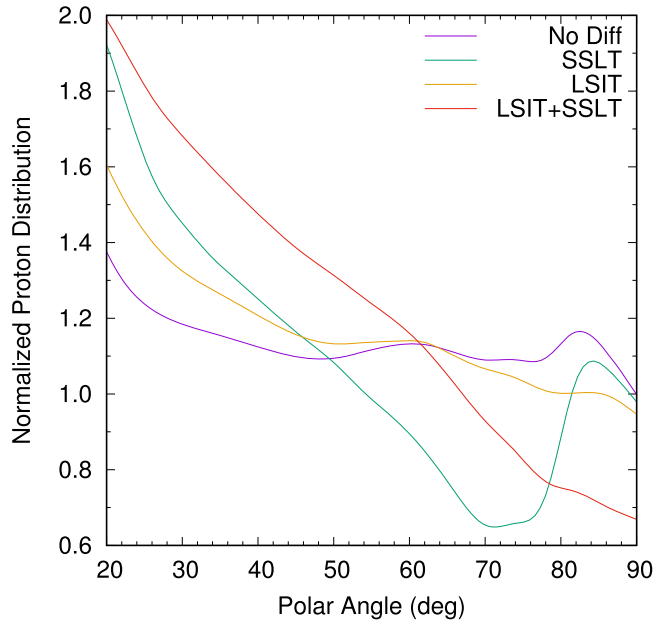

Figure 6. Model distributions of the 1.11 keV protons at the radial distance 198 au that were integrated over pitch angles. The four polar angle profiles are shown: for the case of no pitch angle diffusion of energetic protons (No Diff) and diffusion due to the SSLT only, LSIT only, and composite LSIT+SSLT. All distributions are normalized by the "No Diff" distribution value at the polar angle $\phi = 90^{\circ}$.

observations for both the LSIT and SSLT that have been completed by filling in the data gap in such a way as to create the most difficult situation to survive for the secondary ENA mechanism based on an assumption of weak PUI scattering. The results in the left panel of Figure 7, however, show that the secondary ENA mechanism survives even in this situation because the observed and modeled FWHMs are in good agreement. Otherwise, had we found that $\mathrm{FWHM_{Model}} \gg \mathrm{FWHM_{IBEX}}$, we would have had to conclude that the secondary ENA model does not survive in the framework of the model setup adopted here for the test. So the test results presented in the left panel of Figure 7 support the secondary ENA mechanism based on an assumption of weak PUI scattering in the LISM.

To further assess the performance of our simple model, it is desirable to compare the model and *IBEX* fluxes in addition to the preceding analysis of the ribbon width. The right panel of Figure 7 shows a comparison between the model and *IBEX* fluxes. The shown *IBEX*/Max is the *IBEX* 5 yr averaged ENA flux in the azimuthal cut through $\theta = 51^{\circ}$ in which the peak flux is largest, and *IBEX*/75% is the cut through $\theta = 282^{\circ}$, where the peak flux is 75% of the *IBEX*/Max peak. Two model profiles, "LSIT" and "LSIT+SSLT", are also shown. In the ISMF model used here (see Figure 2), the ENA fluxes always peak in the polar angle directions $\phi = \pm 90^{\circ}$. So, to facilitate the data-model comparison, we align the model and *IBEX*/Max ENA peaks by shifting the model profiles in the polar angle by $18.^{\circ}5$. The diffuse globally distributed heliospheric flux of 90 flux units, which is taken from the work by Schwadron et al. (2014) in the direction toward the peak of *IBEX*/Max, is also added to the model fluxes. The case of "LSIT" is shown here because distribution of PUIs in the ribbon direction is likely to be stable with respect to a generation of the SSLT (Gamayunov et al. 2010; Florinski et al. 2016). This does not contradict the *V1* measurements, because the measured SSLT is at the level of intrinsic magnetometer noise and observed in a different radial direction than the direction toward the *IBEX* ribbon. So it is quite possible that the SSLT is not generated in the ribbon direction. The model peak fluxes are between the *IBEX* peak fluxes in the *IBEX*/Max and *IBEX*/75% cuts, indicating that a "most difficult situation for the secondary ENA mechanism to survive" adopted here for the LSIT and SSLT is close to the real situation in the LISM. The widths of the model profiles around the flux peaks, however, are smaller compared to the *IBEX* widths. This is due to a simplified model for the ISMF used in our simulations. A more realistic magnetic field from the global MHD-plasma/kinetic-neutral model of the heliosphere-LISM interaction has a more realistic draping around the HP. This leads to the broader flux profiles around the peaks, because the width of the polar angle region where $\boldsymbol{B} \cdot \boldsymbol{r} \approx 0$ increases compared to that in our study. Implementation of a more realistic magnetic field, however, is outside of the scope of this study and left for future work.

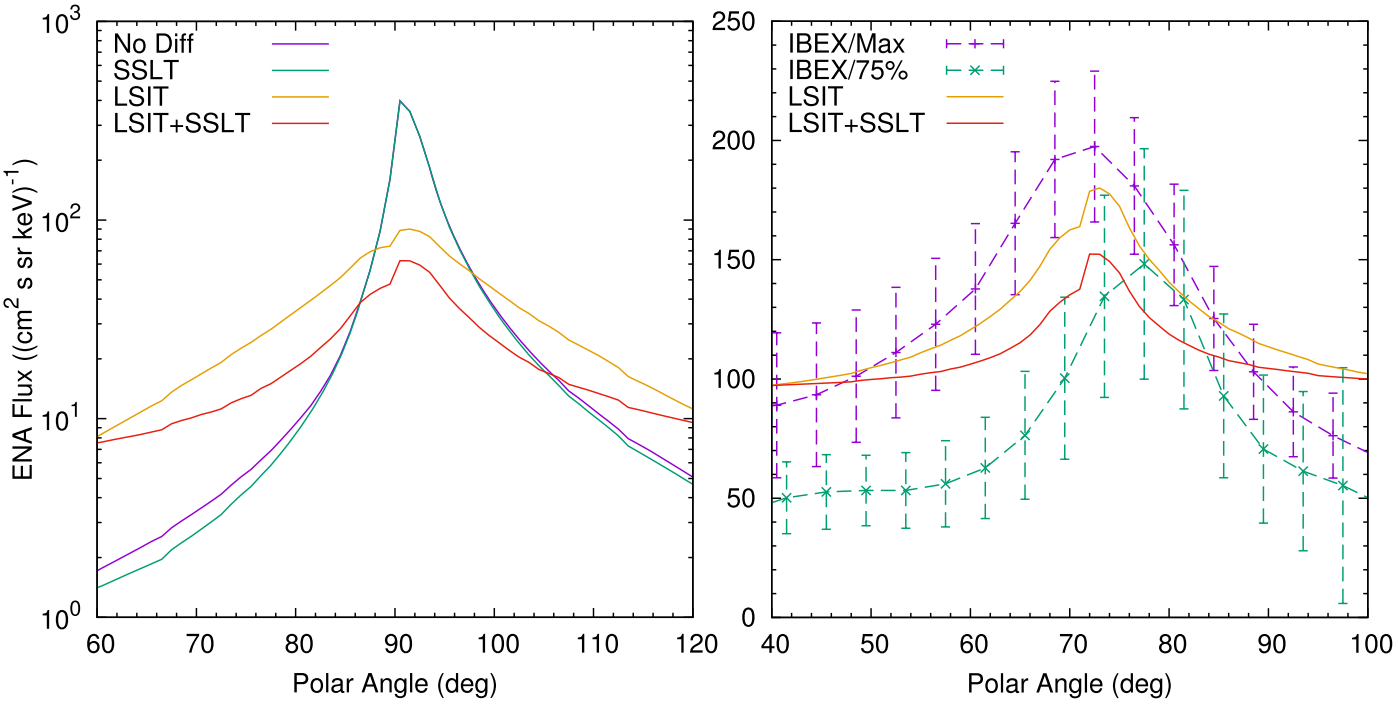

Figure 7. Azimuthal cuts of the 1.11 keV ENA fluxes at the Sun/*IBEX* location vs. polar angle. Left: The four model profiles are shown for the cases of no pitch angle diffusion of energetic protons in the LISM (No Diff) and of diffusion due to the SSLT only, LSIT only, and composite LSIT and SSLT. Right: *IBEX*/Max is the *IBEX* 5 yr averaged ENA flux in the azimuthal cut through $\theta = 51^\circ$ in which the peak flux is largest. *IBEX*/75% is the *IBEX* cut through $\theta = 282^\circ$, where the peak magnitude is 75% of the peak flux in *IBEX*/Max. The error bars show $\pm 2\sigma$, where σ is the standard deviation reported for the data. Two model profiles, "LSIT" and "LSIT+SSLT", are also shown, but now the model profiles are shifted in the polar angle by $18^\circ.5$, and the diffuse globally distributed heliospheric flux of 90 flux units is added.

6. Conclusions

Here we have tested the version of the secondary ENA mechanism of the *IBEX* ribbon formation that is based on an assumption of weak scattering of energetic protons in the LISM. For our test, we have used distributions of the primary ENAs in the LISM obtained from our 3D MHD-plasma/kinetic-neutral model of the heliosphere-LISM interaction. The magnetic field spectrum for the LSIT and an upper limit for the amplitude of SSLT have been taken from the *V1* observations in the LISM. In addition, the results of 1D hybrid simulations of PUIs in the direction toward the *IBEX* ribbon have been used to set the bounding wavenumbers k_1 and k_2 for the SSLT spectrum. Both the LSIT and SSLT spectra constructed for our simulations are likely to cause a stronger pitch angle scattering of PUIs in the region around the 90° pitch angle compared to the scattering in the real conditions of the LISM. Despite this fact, the results of our test support the secondary ENA model that is based on an assumption of weak PUI scattering. Unavoidably, however, our analysis has used some explicit and implicit assumptions. While those assumptions are not strong enough to qualitatively change the major conclusion of our test, we summarize the primary ones along with our comments.

(1) In the kinetic equation for protons, we have neglected the proton convection together with the LISM flow in the direction perpendicular to the ISMF. So we have neglected the accumulation of protons generated farther out and then transported inward by the LISM flow. This, however, is not crucial for the purposes of our study because the ENA fluxes from the ribbon direction ($\boldsymbol{B} \cdot \boldsymbol{r} \approx 0$) are calculated by integrating the proton fluxes over the entire radial extent beyond the HP.

(2) We have used a simplified model for the ISMF. While the model is a quite reasonable approximation for the purpose of our study, a more realistic magnetic field from the MHD-plasma/kinetic-neutral model of the heliosphere-LISM interaction has a more realistic draping around the HP. A more realistic draping results in broader ENA flux profiles around the peaks, because the width of the polar angle region where $\boldsymbol{B} \cdot \boldsymbol{r} \approx 0$ increases compared to that in our study. Using a more realistic magnetic field model will improve the agreement between the model and *IBEX* fluxes, and it will be done in future work.

(3) The distribution function of primary ENAs used here is quite reliable for energies around 1 keV. For these energies, the ENA contribution from a supersonic SW strongly dominates the contribution from the IHS, which can be safely neglected. The ENA radial speed in the SW, by contrast, is determined from the large data set of SW parameters, and the ENA temperature is set on the top of the radial speed using the core SW temperature measurements by *V2* in the supersonic SW.

(4) The fact that *V1* is measuring magnetic field fluctuations in a different radial direction than the direction toward the *IBEX* ribbon does not look to be crucial because the LSIT characteristics are unlikely to depend on the direction, and the SSLT, even if generated in the direction toward the *IBEX* ribbon, is confined in the wavenumber region. This confinement prevents scattering of PUIs with pitch angles around 90° independently of the turbulence intensity. This is exactly what we have adopted for the SSLT model in our analysis.

Finally, we feel obliged to point out a couple of issues that may challenge the "strong scattering" version of the secondary ENA mechanism and so should be addressed in future tests of this

version. (1) The confinement of the SSLT in the wavenumber domain $k \approx [k_1, k_2]$ prevents strong PUI scattering in the region $\boldsymbol{B} \cdot \boldsymbol{r} \approx 0$ where the pitch angles of newly born PUIs are around 90°. The above confinement follows from 1D hybrid simulations of energetic protons in the direction toward the ribbon, and these simulations, of course, do not necessarily include all the physics that operate in reality. However, as far as the bounding wavenumbers exist, the above issue also exists and should be addressed in future tests of the "strong scattering" version. (2) A potential turbulent energy cascade in the region of larger wavenumbers, which is suppressed in the 1D simulations, is unlikely to transport an essential part of the SSLT energy into the region $k > k_2$, because the recent 2D full PIC simulations of the proton ring distribution injected in the direction toward the ribbon show that the dominant modes propagate parallel to the magnetic field and fluctuations progressively migrate from larger to smaller k. These 2D PIC results are in agreement with the 1D hybrid simulations. Note, however, that the referenced PIC results are based on simulations for only a computationally expedient time period, and longer simulation runs may modify the above claim regarding a turbulent energy cascade.

This paper is based on work supported by the National Aeronautics and Space Administration (NASA) under grant number NNX14AP24G.

ORCID iDs

Konstantin V. Gamayunov https://orcid.org/0000-0002-8768-8527

References

Armstrong, J. W., Rickett, B. J., & Spangler, S. R. 1995, ApJ, 443, 209
Barnett, C. F. 1990, Atomic data for fusion, Vol. 1, Collisions of H, H_2, He and Li atoms and ions with atoms and molecules, Tech. Rep. ORNL-6086/VI (Oak Ridge: TN: Oak Ridge Nat. Lab.)
Burlaga, L. F., Florinski, V., & Ness, N. F. 2015, ApJL, 804, L31
Burlaga, L. F., Ness, N. F., Florinski, V., & Heerikhuisen, J. 2014, ApJ, 792, 134
Cannon, B. E., Smith, C. W., Isenberg, P. A., et al. 2014a, ApJ, 784, 150
Cannon, B. E., Smith, C. W., Isenberg, P. A., et al. 2014b, ApJ, 787, 133
Chepurnov, A., & Lazarian, A. 2010, ApJ, 710, 853
Florinski, V., Heerikhuisen, J., Niemiec, J., & Ernst, A. 2016, ApJ, 826, 197
Florinski, V., Zank, G. P., Heerikhuisen, J., Hu, Q., & Khazanov, I. 2010, ApJ, 719, 1097
Funsten, H. O., Allegrini, F., Bochsler, P., et al. 2009a, SSRv, 146, 75
Funsten, H. O., Allegrini, F., Crew, G. B., et al. 2009b, Sci, 326, 964
Funsten, H. O., DeMajistre, R., Frisch, P. C., et al. 2013, ApJ, 776, 30
Fuselier, S. A., Allegrini, F., Funsten, H. O., et al. 2009a, Sci, 326, 962
Fuselier, S. A., Bochsler, P., Chornay, D., et al. 2009b, SSRv, 146, 117
Gamayunov, K. V., & Khazanov, G. V. 1995, PPCF, 37, 1095
Gamayunov, K. V., Zhang, M., Pogorelov, N. V., Heerikhuisen, J., & Rassoul, H. K. 2012, ApJ, 757, 74
Gamayunov, K. V., Zhang, M., & Rassoul, H. 2010, ApJ, 725, 2251
Gruntman, M., Roelof, E. C., Mitchell, D. G., et al. 2001, JGR, 106, 15767
Heerikhuisen, J., Florinski, V., & Zank, G. P. 2005, JGR, 111, A06110
Heerikhuisen, J., Gamayunov, K. V., Zirnstein, E. J., & Pogorelov, N. V. 2016, ApJ, 831, 137
Heerikhuisen, J., & Pogorelov, N. V. 2010, in ASP Conf. Ser. 429, Numerical Modeling of Space Plasma Flows, Astronum-2009, ed. N. V. Pogorelov, E. Audit, & G. P. Zank (San Francisco, CA: ASP), 227
Heerikhuisen, J., Pogorelov, N. V., Florinski, V., Zank, G. P., & le Roux, J. A. 2008, ApJ, 682, 679
Heerikhuisen, J., Pogorelov, N. V., Zank, G. P., et al. 2010, ApJL, 708, L126
Isenberg, P. A. 2014, ApJ, 787, 76
Heerikhuisen, J., Zirnstein, E. J., Funsten, H. O., Pogorelov, N. V., & Zank, G. P. 2014, ApJ, 784, 73
Kennel, C. F., & Petschek, H. E. 1966, JGR, 71, 1
Liu, K., Möbius, E., Gary, S. P., & Winske, D. 2012, JGR, 117, A10102
Livadiotis, G., & McComas, D. J. 2013, SSRv, 175, 183
McComas, D. J., Allegrini, F., Bochsler, P., et al. 2009a, SSRv, 146, 11
McComas, D. J., Allegrini, F., Bochsler, P., et al. 2009b, Sci, 326, 959
McComas, D. J., Alexashov, D., Bzowski, M., et al. 2012, Sci, 336, 1291
McComas, D. J., Allegrini, F., Bzowski, M., et al. 2014, ApJS, 213, 20
McComas, D. J., Bzowski, M., Frisch, P., et al. 2010, JGR, 115, A09113
McComas, D. J., Bzowski, M., Frisch, P., et al. 2015, ApJ, 801, 28
Montgomery, D., Brown, M. R., & Matthaeus, W. H. 1987, JGR, 92, 282
Niemiec, J., Florinski, V., Heerikhuisen, J., & Nishikawa, K.-I. 2016, ApJ, 826, 198
Parker, E. N. 1961, ApJ, 134, 20
Pogorelov, N. V., Zank, G. P., & Ogino, T. 2004, ApJ, 614, 1007
Schlickeiser, R. 1989, ApJ, 336, 243
Schwadron, N. A., & McComas, D. J. 2013, ApJ, 764, 92
Schwadron, N. A., Bzowski, M., Crew, G. B., et al. 2009, Sci, 326, 966
Schwadron, N. A., Moebius, E., Fuselier, S. A., et al. 2014, ApJS, 215, 13
Sokół, J. M., Bzowski, M., Tokumaru, M., Fujiki, K., & McComas, D. J. 2013, SoPh, 285, 167